POLITECNICO DI TORINO
Repository ISTITUZIONALE

Thickness-controlled polyamide membranes via centrifugal thin-film deposition for improved fouling and high-recovery performance

Original
Thickness-controlled polyamide membranes via centrifugal thin-film deposition for improved fouling and high-recovery performance / Jafarian, H., Behzadnia, N., Aghapour Aktij, S., Zandi, Z., Etemadi Maleki, S., Mansourpanah, Y., Arabi Shamsabadi, A., Rahimpour, A., Nejati, S., Tiraferri, A., Sadrzadeh, M., Elliott, M., Dadashi Firouzjaei, M.. - In: NPJ CLEAN WATER. - ISSN 2059-7037. - 9:(2026). [10.1038/s41545-026-00589-0]

Availability:
This version is available at: 11583/3014407 since: 2026-08-13T07:26:49Z

Publisher:
Springer Nature

Published
DOI:10.1038/s41545-026-00589-0

Terms of use:

This article is made available under terms and conditions as specified in the corresponding bibliographic description in the repository

Publisher copyright

(Article begins on next page)

23 October 2026

npj | clean water

Article

Published in partnership with King Fahd University of Petroleum & Minerals

https://doi.org/10.1038/s41545-026-00589-0

Thickness-controlled polyamide membranes via centrifugal thin-film deposition for improved fouling and high-recovery performance

Check for updates

Hesam Jafarian[1], Nima Behzadnia[1], Sadegh Aghapour Aktij[2,3], Zahra Zandi[3], Sanam Etemadi Maleki[1], Yaghoub Mansourpanah[4], Ahmad Arabi Shamsabadi[5], Ahmad Rahimpour[2], Siamak Nejati[6], Alberto Tiraferri[7], Mohtada Sadrzadeh[3] ✉, Mark Elliott[1] ✉ & Mostafa Dadashi Firouzjaei[1,2] ✉

Nanofiltration for desalination and water reuse demands fouling-resistant and high-recovery operation, but is often constrained by permeability–selectivity trade-offs and heterogeneous polyamide growth during interfacial polymerization (IP). Here, we introduce centrifugal thin-film deposition (CTFD) as a controllable aqueous-phase delivery step that spreads piperazine uniformly before polymerization with trimesoyl chloride, limiting monomer infiltration into the porous support and suppressing nonuniform film growth. Molecular dynamics simulations show centrifugal confinement of piperazine near the reaction zone, consistent with experimentally improved film uniformity. CTFD produces ~10–50 nm polyamide layers with lower roughness (R_a ~40–45 nm) than a conventional membrane (R_a ~90 nm). The optimized membrane (0.1 wt.% piperazine; 3.198 kg m/s^2) delivers ~136 LMH flux and 94.3% Na_2SO_4 rejection at 6 bar, fully recovers flux after hydraulic cleaning of sodium alginate fouling, and maintains >85% Na_2SO_4 rejection at high recovery with higher flux. This work offers an effective strategy to tune polyamide layer formation and transport resistance under sulfate-rich nanofiltration conditions where high permeability, fouling reversibility, and high-recovery operation are prioritized.

Water scarcity continues to intensify reliance on desalination and water reuse as dependable water supplies for municipal and industrial demand[1,2]. In these applications, the practical bottleneck is often not the initial separation performance of the membrane, but the ability to maintain stable operation in the presence of organic foulants in saline waters containing divalent ions, which can intensify fouling and complicate cleaning[3]. Membrane fouling remains a primary operational constraint because it increases hydraulic resistance and drives flux decline, requiring more frequent cleaning and making fouling reversibility a key determinant of stable, cost-effective operation[4]. Therefore, for water reuse in particular, where feed composition can fluctuate, and organic loading can be high, membranes that foul reversibly and recover flux after mild hydraulic cleaning are more likely to sustain reliable operation and lower treatment costs[5,6].

In addition, desalination and reuse facilities increasingly pursue high-recovery operation to increase permeate yield and reduce concentrate (brine) volumes and associated management/disposal costs[7]. However, as recovery increases, salt concentrations rise, elevating osmotic pressure and concentration polarization and thereby reducing effective driving force and increasing the sensitivity of flux and rejection to selective-layer transport resistance and pressure-induced compaction[8,9]. Under these high-salinity conditions, even modest differences in selective-layer uniformity and hydraulic resistance can translate into meaningful differences in operating

[1]Department of Civil, Construction, and Environmental Engineering, University of Alabama, Tuscaloosa, AL, USA. [2]Department of Chemical & Materials Engineering, Donadeo Innovation Centre for Engineering, University of Alberta, Edmonton, AB, Canada. [3]Department of Mechanical Engineering, 10-241 Donadeo Innovation Center for Engineering, Advanced Water Research Lab (AWRL), University of Alberta, Edmonton, AB, Canada. [4]Lehrstuhl für Technische Chemie, Universität Duisburg-Essen, Essen, Germany. [5]Department of Chemistry, University of Pennsylvania, Philadelphia, PA, USA. [6]Department of Chemical and Biomolecular Engineering, University of Nebraska Lincoln, Lincoln, Nebraska, USA. [7]Department of Environment, Land, and Infrastructure Engineering, Politecnico di Torino, Turin, Italy. ✉e-mail: sadrzade@ualberta.ca; melliott@eng.ua.edu; mdfirouzjaei@crimson.ua.edu

pressure requirements and flux stability over time[10]. Accordingly, pressure-driven membrane systems should be evaluated not only by initial flux and rejection, but also by (i) fouling reversibility under representative organic foulants and (ii) performance robustness during high-recovery operation under increasing salinity.

Thin-film composite (TFC) nanofiltration membranes are widely applied in desalination and water reuse because they offer high water recovery while selectively rejecting multivalent ions and natural organic matter[11,12]. In typical TFC fabrication, the polyamide selective layer is formed by interfacial polymerization (IP) using an immersion coating of the aqueous amine phase, followed by excess-liquid removal steps before contacting the organic phase[13]. However, instability within the narrow interfacial zone, driven by rapid reaction kinetics and uncontrolled aqueous-phase retention in support pores, can lead to heterogeneous film growth that constrains performance[14,15]. Numerous approaches have been proposed to regulate IP dynamics (e.g., substrate or interlayer engineering[16,17], organic-phase tuning[18], electro-spray-assisted polymerization[19], and molecular layer-by-layer deposition[20]); nevertheless, they often add complexity and cost to membrane fabrication. In piperazine (PIP)-based TFC membranes, the PIP concentration can control the polyamide's thickness, surface morphology, and network structure—key parameters that govern selectivity and stability[21]. Higher PIP uptake can increase crosslinking density, but often promotes nodular growth and higher transport resistance. In contrast, lower PIP concentration can lead to incomplete film formation and heterogeneity[21,22].

However, concentration tuning alone cannot overcome nonuniform monomer distribution, underscoring the need for more precise aqueous-phase delivery to achieve structural control at sub-50 nm. To improve spatial control over the formation of the polyamide film, several alternative monomer delivery strategies have been proposed, including delayed IP via diffusion control[23], vacuum-assisted infiltration[24], reverse interfacial polymerization[25], and in situ additive distribution[26]. While these approaches can modulate interfacial transport, they often rely on imprecise excess-removal steps (such as gravity, rubber rollers, or air knives) that introduce variability and fail to control monomer retention within substrate pores, leading to inconsistent interfacial reactions and nonuniform polyamide morphologies, which are unfavorable for fouling resistance and stable operation under concentrated conditions[27–29].

Here, we introduce centrifugal thin-film deposition (CTFD) as a controllable aqueous-phase delivery step that utilizes radial acceleration to uniformly spread various PIP concentrations across the support before polymerization with trimesoyl chloride (TMC), enabling the formation of highly uniform polyamide selective layers with tunable thickness and morphology[30,31]. This approach can potentially shorten processing time and reduce chemical use by applying centrifugal force to confine and level the aqueous phase across the substrate surface[32]. Membrane performance is evaluated using (i) single-salt filtration, (ii) sodium alginate fouling test emphasizing flux recovery after low-pressure hydraulic cleaning to quantify fouling reversibility, and (iii) high-recovery, open-loop cross-flow filtration to assess stability as concentration increases. Complementary molecular dynamics (MD) simulations provide mechanistic insight into how centrifugal force directs monomer distribution and promotes uniform polyamide formation on the support layer. Together, the experimental and computational results establish a robust structure–property–performance framework for next-generation TFC membranes with improved operability in desalination and water reuse systems.

Results

Optimization of polymer concentration and centrifugal force at dead-end filtration

In the first step, the applicability of the CTFD technique was tested for depositing both aqueous- and organic-phase monomers. Centrifugal application of the organic-phase monomer did not yield a detectable polyamide layer. This is likely due to the low viscosity of the TMC/n-hexane solution (≈ 0.3 mPa·s), which is substantially lower than that of the aqueous PIP phase (≈ 0.9–1.1 mPa·s), resulting in poor retention on the polyethersulfone (PES) surface during coating. Rapid radial displacement of the organic phase likely shortened residence time and limited stable interfacial contact with the aqueous phase, thereby hindering effective polyamide formation. Therefore, subsequent work focused on aqueous-phase deposition.

In conventional IP, the retained aqueous amine phase is strongly influenced by the porous support properties, including wettability, surface roughness, porosity, and pore size, which affect aqueous-solution retention on the surface and within support pores[33]. Additional processing factors, such as gravity drainage and excess-liquid removal, further determine the residual monomer inventory on and within the porous PES support. Consequently, when the organic TMC phase is introduced, local differences in PIP availability and diffusion pathways can lead to heterogeneous reaction zones and nonuniform polyamide growth. In contrast, CTFD modifies the pre-reaction aqueous-phase boundary condition before organic-phase contact, rather than directly altering the intrinsic chemistry of the PIP–TMC reaction. Centrifugal acceleration promotes lateral redistribution of the aqueous phase while simultaneously removing excess solution from the surface and near-surface pores. This process reduces local pooling, limits excessive PIP retention within the porous support, and produces a more controlled residual monomer inventory at the reaction interface. Therefore, the role of CTFD is not simply uniform spreading, but regulation of aqueous-film thickness, monomer residence time, and near-surface PIP availability prior to IP[13,34]. Since polyamide formation is rapid and self-limiting, controlling monomer availability in this narrow time window is critical[35]. This controlled initial condition likely moderates local stoichiometric fluctuations during the subsequent PIP–TMC reaction, enabling thinner and more uniform polyamide formation.

To investigate the influence of monomer concentration and centrifugal force on polyamide structure, four representative membranes were selected to represent the lowest and highest centrifugal forces (A and D) and PIP concentrations (0.5 and 3). Figure 1C schematically illustrates the application of centrifugal force during deposition and the formation of the polyamide layer on the PES substrate. As shown in Fig. S2A and S2B_1–B_4 in the Supporting Information (SI), the N 1 s peak in XPS spectra of all membranes exhibited a prominent peak at 399 eV, which may be attributed to amide nitrogen (–N–C = O)[30]. The survey spectra also showed characteristic peaks at 285.0 eV (C 1 s) and 532.0 eV (O 1 s), which are consistent with typical polyamide chemistry[36]. Moreover, the deconvoluted C 1 s spectra (Fig. 1E_1–E_4) displayed three dominant peaks at 285.2 eV, 286.8 eV, and 288.3 eV, corresponding to C = C/C–C/C–N (aromatic ring in TMC/aromatic ring in TMC/PIP), C–O (carboxylic group in TMC), and C–N/C–O (amide linkages), respectively[36,37].

Top-view FESEM images (Fig. 1A_1–A_4 and Fig. S4B_1–B_3, SI) revealed clear surface-morphology differences as a function of PIP concentrations and centrifugal force. Higher PIP concentrations appeared to lead to more conventional ridge-valley film structures, whereas increased centrifugal forces yielded smoother, more uniform film surfaces. Apparent surface valleys or low-density regions observed in the CTFD images are interpreted as morphology-related features of ultrathin interfacially polymerized polyamide films rather than direct evidence of defects, since top-view imaging alone cannot resolve the full three-dimensional selective-layer structure[38–40]. Accordingly, polyamide formation was evaluated in light of the XPS results presented earlier, together with the cross-sectional electron microscopy discussed below. Moreover, for comparison, the top-view FESEM images of the bare PES support and conventional polyamide membrane are provided in Fig. S4A_1–A_2.

Cross-sectional TEM results (Fig. 1B_1–B_4 and their higher magnification TEM images in Fig. S3A–D, Fig. 1D_1–D_2, and Fig. S4D_1–E_3, SI) showed thin polyamide layers across all CTFD membranes (< 60 nm, Table S1, SI) in comparison to a thicker polyamide selective layer fabricated through the conventional method (Fig. S4C_1, SI) and no visible selective layer for pristine PES supported force, increasing PIP concentration led to a two-fold increase in the polyamide layer thickness from 33.1 nm to 59.9 nm.

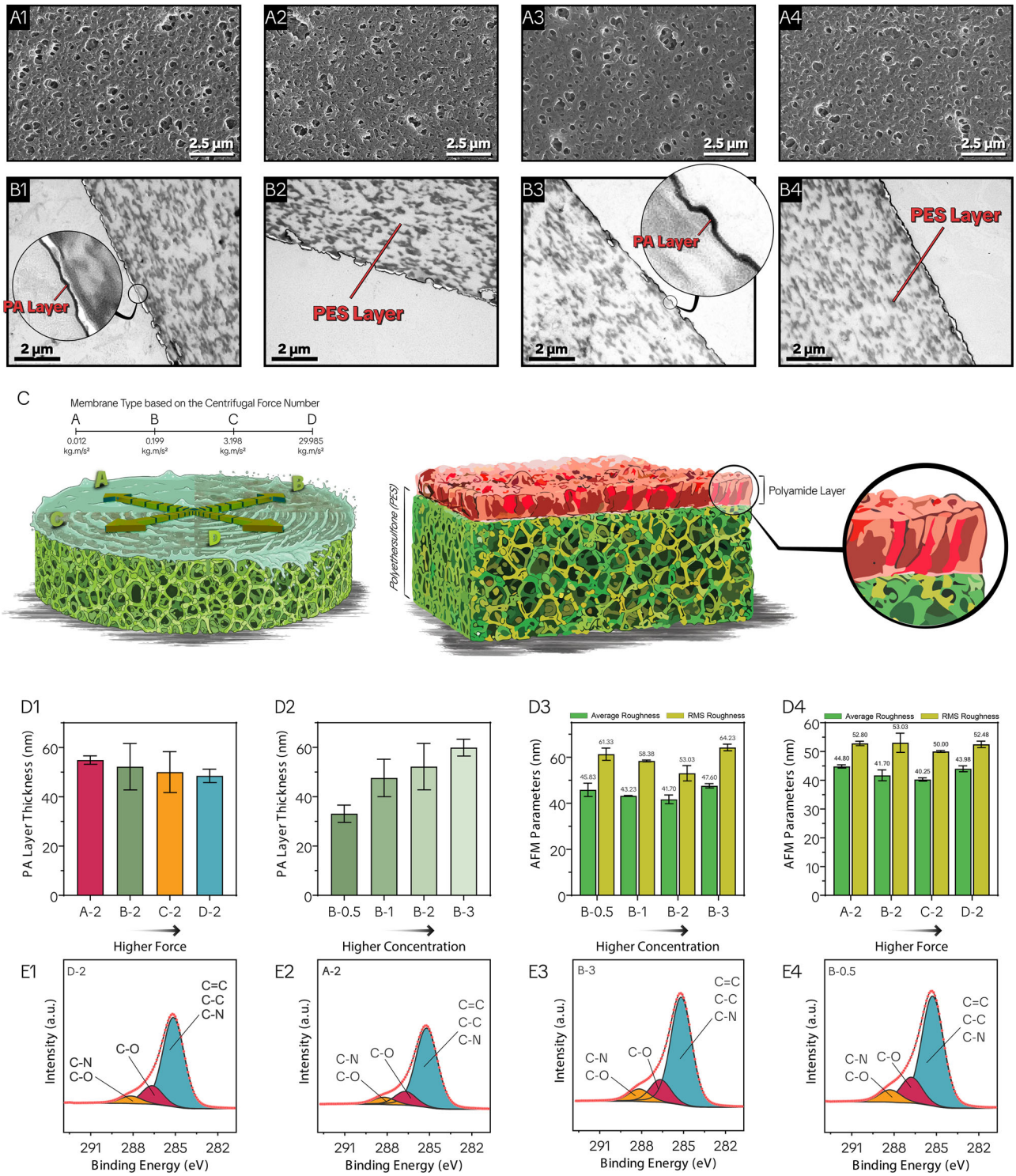

Fig. 1 | Morphological, topographical, and surface chemical characterization of polyamide membranes fabricated with varying piperazine (PIP) concentrations and centrifugal forces (B-0.5, B-3, A-2, and D-2). **A_1–A_4** Top-view FESEM images showing textured morphology of diffusion-limited interfacial polymerization (IP). **B_1–B_4** Cross-sectional TEM images illustrating the formation of thin polyamide selective layers across all CTFD membranes. Thicker layers appeared at higher PIP concentrations, while higher centrifugal forces yielded slightly thinner films. **C** Schematic illustration of the PES substrate showing the application of various centrifugal forces during deposition and the formation of the polyamide selective layer on top. **D_1, D_2** Quantitative analysis of polyamide layer thickness obtained from TEM images using ImageJ, corroborating the observed trend of increasing thickness with PIP concentration and slight reduction with higher centrifugal forces. **D_3, D_4** AFM analysis showing minor roughness variations with increasing PIP concentration (R_a: 45.8–47.6 nm) and negligible changes across different centrifugal forces ($R_a \approx 44$ nm). **E_1–E_4** High-resolution C 1 s spectra deconvoluted into peaks for C = C/C–C/C–N, C–O, and C–N/C–O, indicating amide bond formation across all fabrication conditions.

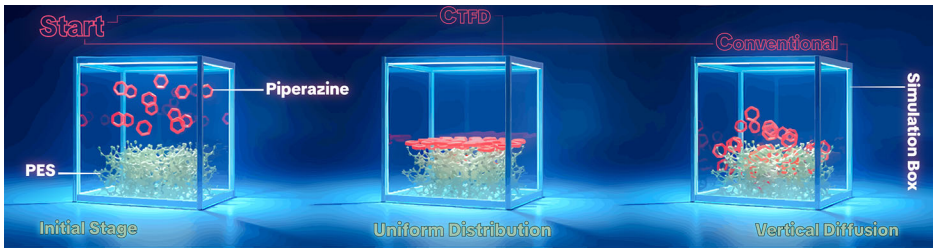

Fig. 2 | Molecular dynamics simulation. Final distribution of piperazine (PIP) monomers on the polyethersulfone (PES) substrate after molecular dynamic simulation for CTFD and conventional techniques. The centrifugal deposition configuration appeared to promote enhanced monomer uniformity and surface coverage compared to the disordered distribution observed in the conventional approach.

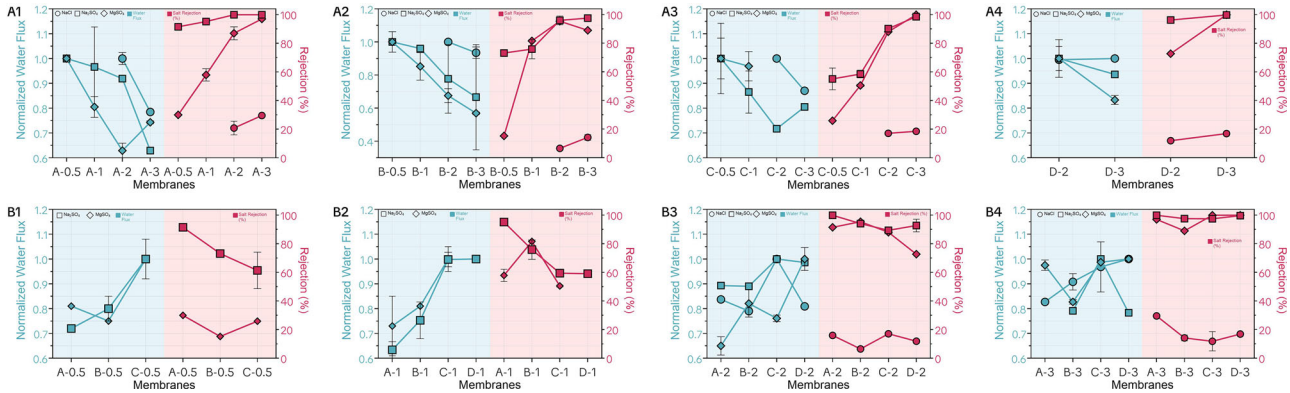

Fig. 3 | Dead-end filtration performance of TFC membranes under varying fabrication parameters. A_1–A_4 Normalized water flux and salt rejection for Na_2SO_4, $MgSO_4$, and NaCl as a function of piperazine (PIP) concentration at fixed centrifugal forces. **B_1–B_4** Normalized water flux and salt rejection for Na_2SO_4, $MgSO_4$, and NaCl as a function of centrifugal force at fixed PIP concentrations. Increasing PIP concentration decreased flux but enhanced rejection, whereas increasing centrifugal force generally improved flux, with rejection trends depending on salt type and PIP loading.

In contrast, at fixed PIP concentrations, increasing centrifugal forces resulted in reduced film thickness. AFM topography (Fig. 1D_3–D_4) revealed minimal variations in surface roughness for the membranes fabricated via CTFD. At fixed centrifugal force, R_a increased slightly from 45.8 nm to 47.6 nm as PIP concentration increased. Similarly, in the centrifugal force series at fixed PIP concentrations, R_a values remained nearly constant at ≈ 44 nm. Notably, all CTFD membranes exhibited significantly lower roughness than the conventional membrane (R_a ≈ 90 nm), resulting in smoother surfaces that are hypothesized to promote more uniform flow distribution and enhance antifouling performance[41].

Figure 2 compares the molecular distribution of PIP monomers on PES substrates for conventional dip-coating and CTFD methods, as simulated in LAMMPS. The simulation was designed not to replicate the full IP reaction but to isolate the mechanical influence of centrifugal acceleration on monomer transport and surface distribution. In the conventional deposition model, PIP molecules displayed a disordered, subsurface arrangement, characteristic of diffusion-dominated transport and random aggregation, conditions that may lead to nonuniform reaction zones and heterogeneous polyamide structures[42]. In contrast, centrifugal deposition directed PIP molecules radially into a compact, homogeneous boundary layer, enhancing monomer confinement and improving surface coverage. These results align with SEM, TEM, and AFM observations, which showed that CTFD membranes possessed uniform, thin selective layers with reduced surface roughness. More information on the MD simulation can be found in the SI.

To summarize, characterization results for CTFD membranes showed that increasing PIP concentration led to thicker polyamide layers with ridge structures, whereas increasing centrifugal force mainly reduced film thickness and yielded more uniform films. Furthermore, surface roughness remained largely unchanged as long as a centrigufal force was applied. Centrifugal acceleration in the CTFD process may stabilize the interface in IP by balancing monomer diffusion and polymerization rates, minimizing concentration fluctuations, and ensuring uniform, thin polyamide formation[43]. To assess the influence of these structural changes on membrane performance, CTFD membranes were first evaluated in a dead-end filtration setup.

Figure 3 summarizes normalized water flux and observed salt rejection results for Na_2SO_4, $MgSO_4$, and NaCl as functions of PIP concentration and centrifugal force. At fixed centrifugal force (Fig. 3A_1–A_4), all membranes showed maximum normalized flux at the lowest PIP loading, followed by a steady decline as PIP concentration increased. At the same time, salt rejection for Na_2SO_4, $MgSO_4$, and NaCl all increased with higher PIP concentrations. For example, in Na_2SO_4 filtration, increasing PIP from 0.5 wt.% to 3 wt.% at a fixed 0.199 kg m/s^2 (Fig. 3A_2) reduced normalized flux by 43.1% (from 1.00 to 0.569), while increasing rejection by 24.4% (from 73.2% to 97.6%). These trends reflect the classic permeability–selectivity trade-off, likely driven by the formation of thicker polyamide layers at higher PIP concentrations, which enhance salt rejection but increase transport resistance[44]. At fixed PIP concentration (Fig. 3B_1–B_4), higher centrifugal force generally enhanced normalized flux, consistent with resulting in a thinner film, as observed in TEM analyses. For example, in Na_2SO_4 filtration, increasing centrifugal force from 0.012 kg m/s^2 to 29.985 kg m/s^2 at a fixed 2 wt.% PIP (Fig. 3B_3) increased the normalized flux by approximately 54% (from 0.65 to 1.00). Rejection trends, however, varied across salts and PIP loadings, reflecting an interplay between reduced thickness, which may translate into lower selectivity[12].

Evaluation of cross-flow filtration and extended characterization

The dead-end filtration tests revealed general trends in permeability and salt rejection across the investigated PIP concentrations and centrifugal forces, while also highlighting the expected trade-off between reduced transport resistance and salt selectivity. To clarify the selection logic, a trade-off matrix summarizing water flux, Na_2SO_4 rejection, TEM-derived polyamide thickness, and AFM roughness is provided in Table S6, SI. This screening did not identify a universally superior centrifugal force based on rejection alone; rather, it showed that 3.198 kg m/s^2 provided a suitable baseline condition for the next-stage PIP optimization because it generally produced

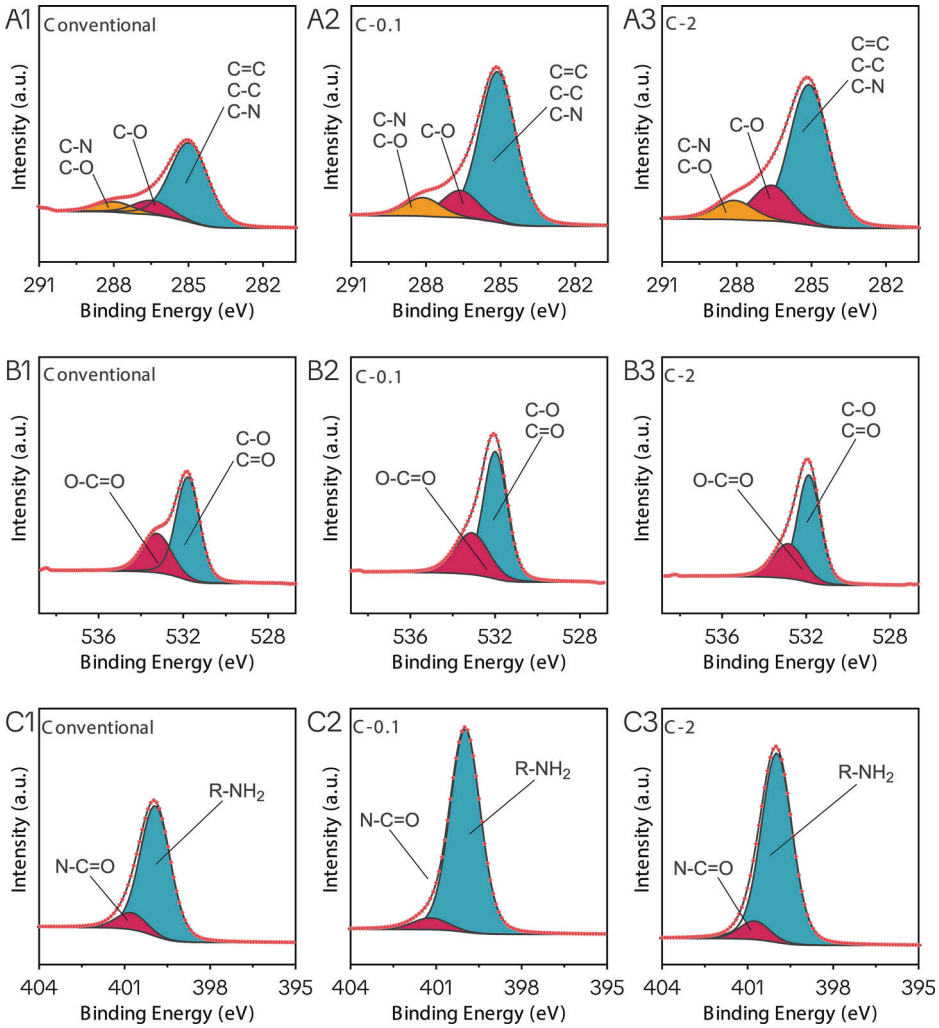

Fig. 4 | Surface chemistry analysis of the conventional, C-0.1, and C-2 membranes, respectively. Deconvoluted high-resolution XPS spectra of (**A_1–A_3**) C 1 s, (**B_1–B_3**) O 1 s, and (**C_1–C_3**) N 1 s show the characteristic chemical bonding associated with amide formation.

thinner and smoother polyamide layers with lower transport resistance, while allowing the effect of monomer concentration on film formation to be more clearly resolved. Therefore, 3.198 kg m/s^2 was selected as the baseline centrifugal force for the refined cross-flow study. Unlike the dead-end filtration tests, which employed four PIP concentrations (0.5, 1, 2, and 3 wt.%), the cross-flow filtration study explored a lower and more finely resolved PIP concentration range (0.05–2 wt.%) to capture subtle effects of monomer availability on membrane formation and performance.

XPS analysis was performed to examine the surface elemental composition and chemical bonding of the conventional membrane and two CTFD membranes prepared with low (0.1 wt.%) and high (2 wt.%) PIP concentrations. The survey spectra (Fig. S6A, SI) showed peaks at 285 eV (C 1 s), 532 eV (O 1 s), and 399 eV (N 1 s), characteristic of polyamide chemistry. High-resolution C 1 s spectra (Fig. 4A_1–A_3) displayed peaks at 285 eV (C–C/C = C from TMC/aromatic rings and C–N from PIP), 286.5 eV (C–O from carboxylic acid groups in unreacted or hydrolyzed TMC), and 288.1 eV (C–N and C–O in amide linkages)[36,37]. High-resolution O 1 s spectra (Fig. 4B_1–B_3) exhibited peaks at 531.8 eV from carbonyl groups in amides (N–C = O) and possibly hydroxyls, and at ~533.3 eV from O–C = O in carboxylic acids, likely formed via hydrolysis of residual TMC acyl chlorides[45]. High-resolution N 1 s spectra (Fig. 4C_1–C_3) revealed two components at 399.9 eV from terminal amine groups (R–NH_2) and 400.8 eV from amide nitrogen (N–C = O)[46]. High-resolution C1s, N1s, and O1s spectra for the remaining membranes are provided in Fig. S6B_1–D_5, SI.

Table S4, SI presents the atomic composition of the conventional and CTFD membranes, from which O/N ratios were calculated to assess the crosslinking degree, as determined by XPS analysis. A fully crosslinked polyamide has an ideal O/N ratio of 1.00. The conventional membrane exhibited an O/N ratio of 2.11, indicating incomplete crosslinking and the presence of hydrolyzed species. The membrane prepared with low PIP concentration (0.1 wt.%) showed an even higher O/N ratio (2.49), suggesting a relatively low apparent crosslinking degree, likely due to limited monomer availability. In contrast, the membrane fabricated with high PIP concentration (2 wt.%) exhibited a lower ratio (1.78), indicating a more highly crosslinked network. Complementary EDX analysis (Table S5, SI) aligned with these findings, showing increased nitrogen content and reduced oxygen content at higher PIP concentrations, consistent with enhanced crosslinking.

The impact of PIP concentration on membrane performance was evaluated via closed-loop cross-flow filtration using Na_2SO_4 as a model salt (Fig. 5A). Consistent with dead-end filtration results, a clear inverse relationship between PIP concentration and water flux was observed. At low PIP concentration (0.1 wt.%), the water flux reached 136.1 ± 8.7 LMH, approximately 184% higher than the conventional membrane (47.9 ± 6.2 LMH) and 25.5% higher than the NF270 benchmark (108.4 ± 5.8 LMH). These high permeabilities are primarily attributed to the thinner selective layers formed at low PIP concentrations, as evidenced by cross-sectional TEM (Fig. 5E_1–E_3), which showed that the membrane prepared with low PIP concentration (0.1 wt.%) formed a ~ 15 nm layer, compared to the thicker (~92 nm), nonuniform film observed in the conventional membrane[47]. Cross-sectional FESEM images (Fig. 5D_1–D_3) showed a comparable difference in polyamide thickness, in agreement with the TEM

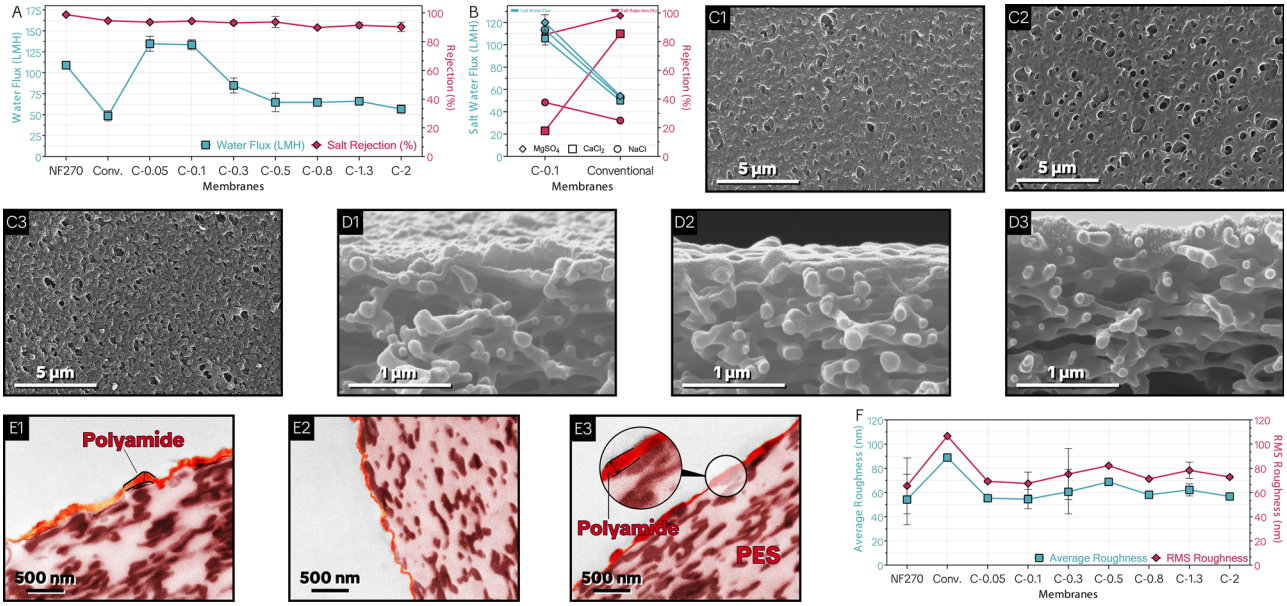

Fig. 5 | Filtration performance and structural analysis of membranes fabricated under a centrifugal force of 3.198 kg m/s^2 with varying piperazine (PIP) concentrations. A Water flux and Na_2SO_4 rejection for all membranes. **B** Salt water flux and rejection for other salts ($MgSO_4$, $CaCl_2$, and NaCl) were evaluated only for the conventional membrane and the optimized CTFD membrane (C-0.1). **C_1–C_3** Top-view FESEM images for the conventional, C-0.1, and C-2 membranes, respectively, showing smoother, less textured surfaces at lower PIP loadings (e.g., 0.1 wt.%) and ridge-like patterns at higher concentration (2 wt.%); (**D_1–D_3**) Cross-sectional FESEM images and (**E_1–E_3**) cross-sectional TEM images for the conventional, C-0.1, and C-2 membranes, respectively, showing a significantly thinner selective layer for membrane fabricated at 0.1 wt.% (14.7 nm) versus the conventional membrane (91.7 nm); (**F**) AFM parameters showing reduced surface roughness for membrane fabricated at 0.1 wt.% compared to conventional membrane, with corresponding R_a and RMS values.

observations. AFM results (Fig. 5F) revealed a smoother surface (R_a: 54.5 nm) for the CTFD membrane (C-0.1), compared to the conventional membrane (R_a: 88.9 nm). The reduced roughness likely reflects moderated local monomer excess and more uniform early-stage interfacial polymerization under centrifugal deposition. Top-view FESEM images (Fig. 5C_1–C_3) also showed minimal ridge formation at low PIP loading, in contrast to the rough, ridge-rich surface of the conventional membrane. Collectively, the thin and smooth layer formed at lower monomer concentrations likely reduced transport resistance and facilitated water passage[43,48].

As PIP concentration increased, water flux declined steadily, dropping to 61.8 ± 10.9 LMH at 2 wt.%, approximately 54.6% lower than the flux observed at 0.1 wt.% PIP. TEM analysis of the membrane prepared with 2 wt.% PIP revealed a thicker (~47 nm) film. Supplementary data (Fig. S6E_1–E_5 and Table S1, SI) showed a monotonic increase in film thickness with increasing PIP concentration, likely driven by intensified monomer reactivity and crosslinking. AFM analysis revealed a non-monotonic roughness trend with R_a peaking at ~0.5 wt.% PIP before declining at higher loadings (R_a: 58.3 nm at 2 wt.%), likely due to smoother polyamide deposition once surface reactivity became saturated, limiting further ridge development[49].

To further assess filtration performance, the optimized CTFD membrane (0.1 wt.% PIP) and the conventional membrane were evaluated in cross-flow filtration using individual $MgSO_4$, $CaCl_2$, and NaCl as representative divalent and monovalent salts. The CTFD membrane exhibited more than twice the water flux of the conventional membrane across all three salts (Fig. 5B), reflecting its thin, smooth, and uniform selective layer.

The crosslinking and morphological differences help explain the observed trends in salt rejection (Fig. 5A, B). For Na_2SO_4, rejection remained high at ~93–94.5% across low to moderate PIP concentrations, suggesting that even with reduced apparent crosslinking, the thin selective layers maintained sufficient structural integrity to reject sulfate ions effectively. Sulfate behaves as the co-ion and experiences strong Donnan exclusion because of its divalent charge and hydrated nature, making its transport through the negatively charged polyamide layer unfavorable. The slight decrease in Na_2SO_4 rejection to ~90.3% for the membrane fabricated at 2 wt.% PIP, despite its higher apparent crosslinking degree, indicates that sulfate rejection was not governed by crosslinking degree alone. At excessive PIP concentration, the IP reaction may proceed too rapidly, promoting polyamide overgrowth and a more pronounced ridge-structured morphology, which may generate a less favorable nanoscale selective network despite the thicker and more crosslinked average structure[38,50]. $MgSO_4$ rejection decreased moderately (from 98.1% in the conventional membrane vs. 84.9% in the CTFD membrane). In contrast to Na_2SO_4, Mg^{2+} can reduce the effective electrostatic exclusion of sulfate by locally screening membrane charge and changing the Donnan potential within the active layer. $MgSO_4$ rejection is thus more sensitive to the morphology and thickness of the selective layer[51].

For $CaCl_2$, the rejection decline was more pronounced (85.47% for the conventional membrane vs. 17.83% for the CTFD membrane). $CaCl_2$ behaves differently because the co-ion is now Cl^-, which is monovalent and therefore experiences much weaker Donnan exclusion than sulfate. Once co-ion exclusion is weak, any reduction in size exclusion mechanisms can cause a large increase in $CaCl_2$ passage[52]. Furthermore, zeta potential measurements (Fig. S7) showed that both the conventional and C-0.1 membranes remained negatively charged across the tested pH range, with the C-0.1 membrane exhibiting slightly more negative values than the conventional membrane. This indicates that the lower $MgSO_4$ and $CaCl_2$ rejection of C-0.1 did not arise from loss of surface charge. Instead, the results support a combined mechanism in which preserved electrostatic exclusion maintains sulfate rejection, whereas the thinner and lower-crosslinked selective layer exerts a stronger influence on salts subject to weaker Donnan exclusion. In contrast, NaCl rejection was enhanced modestly, increasing from 24.97% for the conventional membrane to 37.6% for the CTFD membrane. For NaCl, size- and charge-based discrimination is weak because both ions are small and monovalent. The measured NaCl rejection is therefore strongly influenced by defect-mediated transport, e.g., pinholes, locally under-formed regions, ridge–valley hot spots, and other non-selective pathways. A thinner but more uniform film can thus reject NaCl better than a more heterogeneous film[38,48].

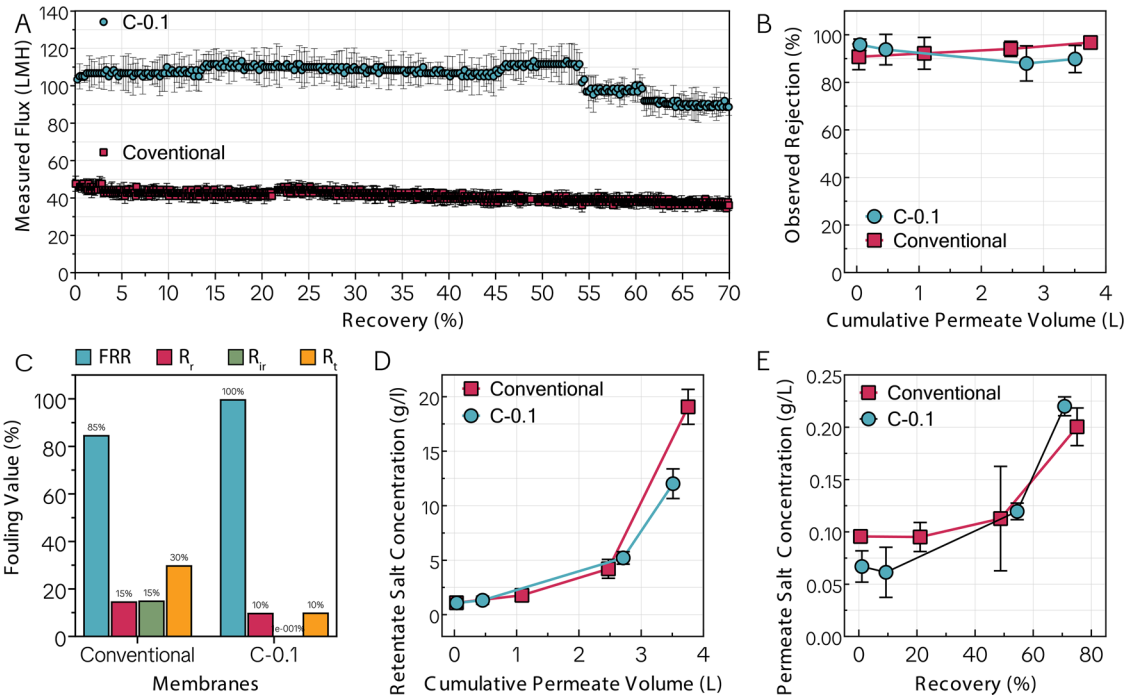

Fig. 6 | High-recovery and fouling performance of the conventional and CTFD membranes. A, **B**, **D**, **E** High-recovery open-loop cross-flow filtration performance of conventional and CTFD membranes using Na_2SO_4 feed solution. **A** Measured flux as a function of recovery, showing the higher and more stable flux of the CTFD membrane compared to the conventional one. **B** Observed rejection as a function of cumulative permeate volume, where the conventional membrane exhibits a gradual increase in rejection while the CTFD membrane shows minor variability. **C** Antifouling performance of the conventional and CTFD membranes during sodium alginate (200 mg/L) filtration, showing fouling parameters following a complete low-pressure cleaning cycle. **D** Retentate salt concentration as a function of cumulative permeate volume, illustrating faster concentration buildup for the conventional membrane. **E** Permeate salt concentration as a function of recovery, showing slightly higher values for the CTFD membrane at elevated recoveries due to its higher permeability.

High-recovery and fouling performance

To further assess performance under practical desalination conditions, both the conventional and CTFD membranes were tested in a high-recovery, open-loop cross-flow filtration system. As shown in Fig. 6A, B, D, E, measured flux, observed rejection, and salt concentrations were monitored as cumulative permeate volume and system recovery increased. The CTFD membrane exhibited a high initial flux (~103 LMH), which gradually declined as osmotic pressure and concentration polarization increased in the open-loop filtration setup[8]. Despite this moderate decline at higher recoveries, the CTFD membrane consistently maintained a higher flux than the conventional membrane (~47.6 LMH initially), which remained relatively stable throughout the test (Fig. 6A), highlighting the advantage of the ultrathin and uniform polyamide layer, which, despite its lower apparent crosslinking degree, maintained adequate selectivity while reducing transport resistance.

For observed rejection (Fig. 6B), both membranes maintained high Na_2SO_4 rejection (>85%) throughout the test. The conventional membrane showed a slight upward trend, increasing from roughly 90.6% to ~96.8%, indicating a gradual enhancement in rejection attributed to reduced effective pore size as the test progressed, due to compaction and reduced electrostatic swelling at higher ionic strength. In contrast, the CTFD membrane showed greater variability, with rejection decreasing from 95.8% to 88% before partially recovering to 89.8%, due to a different balance among concentration polarization, osmotic pressure rise, and mechanical compaction. A smoother, more uniform film should distribute transmembrane pressure more evenly, avoiding localized stress at thin ridge valleys. While this would not reduce compaction per se, it may reduce localized over-compaction of the smoother film obtained through CTFD. As shown in Fig. 6D, retentate salt concentration increased with cumulative permeate volume for both membranes, reflecting progressive feed concentration. However, the conventional membrane exhibited a steeper rise, reaching ~20 g/L compared to ~13 g/L for the CTFD membrane, consistent with its lower water flux and slower dilution of retained salts. Figure 6E shows that permeate salt concentration remained generally low for both membranes but was slightly higher for the CTFD membrane, particularly at higher recoveries (≥60%), indicating a modest trade-off between its enhanced permeability and ion selectivity. Overall, the CTFD membrane maintained a more stable and elevated flux while sustaining high rejection performance and suitable permeate quality, demonstrating superior hydraulic performance and reduced concentration polarization, despite minor selectivity fluctuations at higher recoveries.

To verify the structural stability of the ultrathin C-0.1 selective layer after high-recovery operation, post-mortem TEM and AFM analyses were performed before and after Na_2SO_4 high-recovery test (Fig. S8, SI). Cross-sectional TEM confirmed that the C-0.1 polyamide layer remained continuous and retained its ultrathin thickness after testing, with no obvious delamination, collapse, or measurable thinning in the examined regions. AFM analysis further showed that the C-0.1 surface did not undergo roughening after high-recovery filtration. These post-mortem results support that the observed flux and rejection variations were mainly associated with transport-related effects, including concentration polarization, increased osmotic pressure, and possible compaction, rather than selective-layer damage.

The fouling behavior of the conventional and CTFD membranes was preliminarily assessed using sodium alginate as a model foulant. As shown in Fig. 6C, the CTFD membrane exhibited full flux recovery after low-pressure hydraulic cleaning, indicating minimal irreversible foulant adhesion and enhanced flux due to the removal of weakly bound foulants[53]. Because the operating pressure for each membrane was adjusted to achieve the same initial flux, differences in fouling behavior can be attributed primarily to surface and structural properties rather than hydraulic loading. The high flux recovery ratio of the CTFD membrane indicates that foulant accumulation was predominantly reversible, suggesting weak foulant adhesion and limited pore or surface blockage. This behavior is consistent

with the smooth and structurally uniform polyamide layer formed via the CTFD technique, which reduced the presence of localized high-flux regions and surface valleys that may act as fouling initiation sites[3,54–57]. To further address fouling resistance under a more representative organic-fouling condition, an additional mixed-foulant test was conducted using sodium alginate, bovine serum albumin, and humic acid in the presence of NaCl and $CaCl_2$ (Fig. S9, SI). The C-0.1 membrane again showed substantially improved fouling reversibility, with an FRR of 99.4% and irreversible fouling of only 0.6%, compared with 83.5% FRR and 16.5% irreversible fouling for the conventional membrane. These results confirm that the improved antifouling behavior of C-0.1 was retained under a more complex synthetic organic-fouling challenge.

Discussion

In conclusion, this work demonstrates CTFD as a simple aqueous-phase delivery step to improve the uniformity of IP-formed polyamide layers in nanofiltration membranes. By controlling PIP distribution before reaction with TMC, CTFD produced thinner and smoother selective layers and enabled systematic tuning by centrifugal force and PIP concentration. Under the optimized condition (0.1 wt.% PIP, 3.198 kg m/s^2), the membrane delivered high flux (~136 LMH at 6 bar) with high Na_2SO_4 rejection. Importantly for desalination and reuse applications, performance was evaluated beyond initial flux–rejection: (i) in sodium alginate fouling tests, the CTFD membrane showed full flux recovery after mild hydraulic cleaning, indicating predominantly reversible fouling consistent with a smoother, more uniform surface; and (ii) in high-recovery cross-flow operation with increasing Na_2SO_4 concentration, the CTFD membrane sustained substantially higher flux than the conventional membrane while maintaining >85% observed rejection. MD simulations supported the mechanism by indicating centrifugal confinement of PIP near the interface, consistent with the reduced heterogeneity observed experimentally. While the present CTFD configuration is batch-based, the underlying principle of force-regulated monomer confinement is compatible with emerging coating-assisted and roll-to-roll interfacial polymerization strategies, providing a pathway toward scalable membrane fabrication[58–60]. Overall, CTFD provides a practical route to improve fouling reversibility and high-recovery robustness under sulfate-dominated nanofiltration conditions, while also highlighting the permeability–selectivity tradeoff that can emerge for salts such as $MgSO_4$ and $CaCl_2$ when ultrathin, lower-crosslinked polyamide layers are formed.

Methods

Materials

PIP (>99%) anhydrous, TMC (>98%), triethylamine (TEA), and n-hexane (>95%) were purchased from Sigma-Aldrich for the synthesis of the polyamide selective layer by IP reaction. A commercial PES membrane (Sterlitech Co., pore size 0.03 µm, thickness 110–150 µm) was used as received. A commercial NF270 membrane (DuPont, DE, USA) was purchased and used as a benchmark for performance comparison. Sodium sulfate (Na_2SO_4, 99.5%), sodium chloride (NaCl, >99.5%), calcium chloride ($CaCl_2$, 96%), magnesium sulfate ($MgSO_4{\cdot}6H_2O$, 99%), sodium bicarbonate ($NaHCO_3$), and sodium alginate ($NaC_6H_7O_6$) were also purchased from Sigma-Aldrich and used to prepare the feed solutions for filtration tests. All solutions and rinsing steps were prepared using deionized (DI) water.

Membrane Fabrication and Characterization

The conventional TFC membrane (control) was fabricated on a commercial PES substrate. The substrate was immersed in an aqueous amine solution containing 2 wt.% PIP and 0.4 wt.% TEA, in DI water for two minutes. TEA concentration was kept constant at 0.4 wt.% across all membranes to isolate the effects of PIP concentration and centrifugal force, which were the only variables investigated in this study. TEA served as an acid scavenger to neutralize the HCl generated during the IP reaction, and maintaining a constant concentration minimized additional effects on polyamide formation[61]. After immersion, the excess amine solution was removed using a rubber roller three times. The membrane was subsequently immersed in n-hexane containing 0.1 wt.% TMC, and left for 30 seconds to allow for the formation of the polyamide selective layer via IP reaction. The resulting membrane was heat-treated at 70°C for 10 minutes to promote crosslinking and stabilize the polyamide network.

For the fabrication of CTFD membranes, a commercial PES substrate was first fixed onto the stationary disc of a coating device (Fig. S1, SI). To investigate the effect of centrifugal force, an aqueous solution containing various concentrations of PIP at the selected concentrations, with TEA fixed at 0.4 wt.%, was deposited onto the substrate. Then, the disc was set into rotation to enable centrifugal spreading. Once the desired centrifugal force was applied, it spread the aqueous monomer solution radially outward, promoting uniform monomer distribution and efficient removal of excess solution without the need for mechanical rolling. Following centrifugal deposition, the membrane was immediately immersed in an organic solution comprising 0.1 wt.% TMC dissolved in n-hexane for 30 s to initiate the IP reaction. After polymerization, the membrane underwent thermal treatment at 70 °C for 10 min to enhance crosslinking and ensure structural stability. All fabricated membranes were then stored in DI water at 4 °C for further characterization and performance evaluation. Figure 7 presents the schematic illustration of the IP process utilized for fabricating polyamide membranes. In this study, the centrifugal force values (kg m/s^2) and PIP concentration were considered as variables to fully optimize the CTFD Process (Table S2, SI).

The surface and cross-sectional morphology of the membranes were examined using field-emission scanning electron microscopy (FESEM; Apreo, Thermo Fisher Scientific, USA) equipped with an energy-dispersive X-ray (EDX) spectrometer, operated at 30 kV. Before imaging, the membranes were coated with a 5 nm gold layer using a sputter coater (Leica EM ACE600, USA). Transmission electron microscopy (TEM; Philips/FEI Morgagni 268, USA) was used to analyze the cross-sectional morphology of the membranes. The surface chemistry of the membranes was investigated using X-ray photoelectron spectroscopy (XPS) using a Kratos AXIS ULTRA system. The surface topography was characterized using atomic force microscopy (AFM; Bruker Dimension Icon, USA) over a 10 µm × 10 µm area. Moreover, the roughness parameters (average roughness, R_a, and root-mean-square roughness, RMS) were calculated using Gwyddion software, version 2.62. Zeta potential was determined using Anton Paar SurPASS electrokinetic solid surface potential analyzer (Anton Paar USA, Ashland, VA).

Filtration Experiments

Membrane performance was assessed using both dead-end and cross-flow filtration systems. Dead-end tests were performed at five bar using a stirred cell (47 mm diameter) and 1000 mg/L solutions of Na_2SO_4, $MgSO_4$, and NaCl. Membranes were pre-compacted with DI water at six bar for 30 minutes before testing. Although membranes fabricated at lower centrifugal forces exhibited comparable rejection performance, operation at 3.198 kg m/s^2 yielded the most consistent flux and rejection across replicate samples. Therefore, this value was chosen as the baseline centrifugal force for systematic evaluation under cross-flow conditions, where operational stability and reproducibility are critical. Cross-flow filtration was performed using a lab-scale system with a 22 cm^2 membrane cell. The cross-flow rate was one LPM, the operating pressure was six bar, and the feed temperature was maintained at 25 ± 1 °C. Membranes were pre-compacted at eight bar for six hours. Permeate flux (J_W) and salt rejection were measured using 1000 mg/L aqueous solutions of Na_2SO_4, $MgSO_4$, $CaCl_2$, and NaCl. Permeate flux was calculated using[8]:

$$J_W = V / A\,t \tag{1}$$

where J_W is the saltwater flux (LMH), V is the volume of permeate collected (L), A is the effective membrane area (m^2), and t is the filtration time (h). Salt

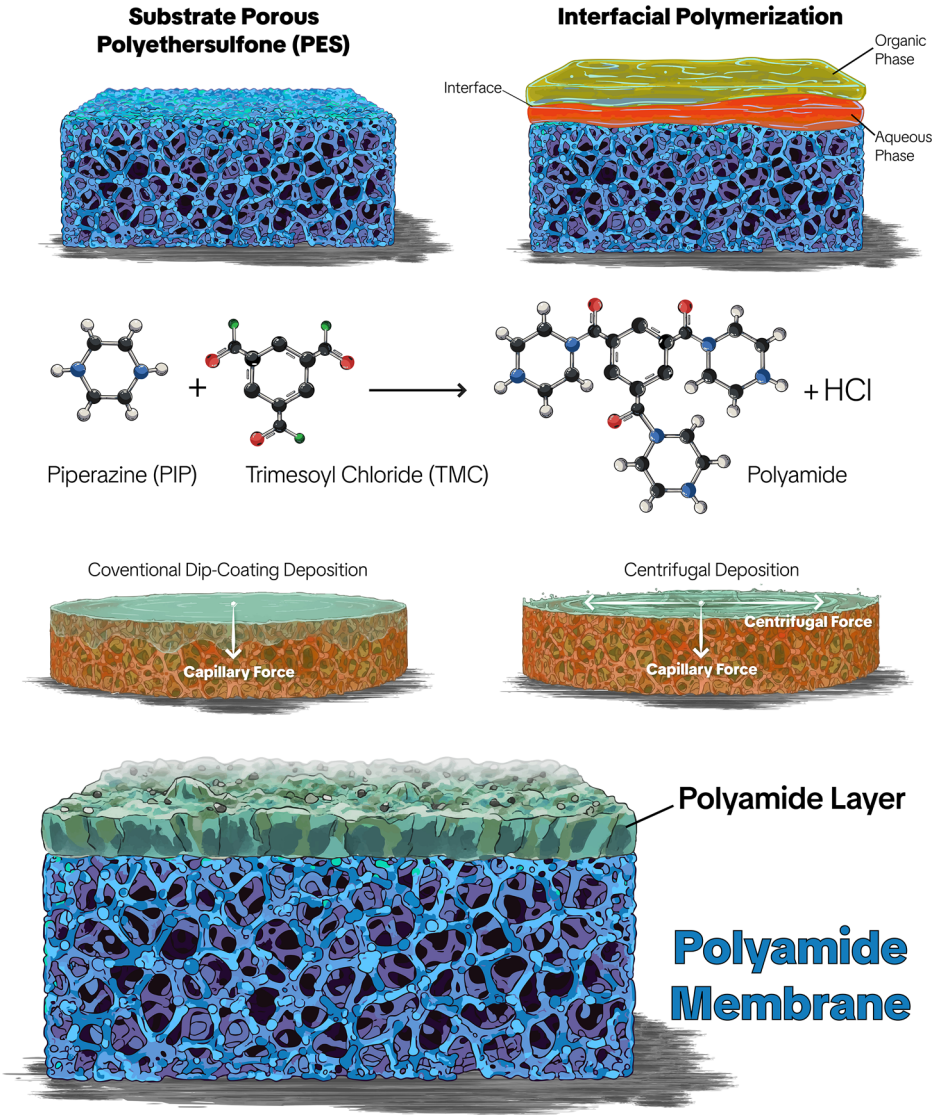

Fig. 7 | Fabrication process for a polyamide thin-film composite (TFC) membrane. A Polyethersulfone (PES) substrate is first coated with an aqueous piperazine (PIP) solution, followed by contact with an organic phase containing trimesoyl chloride (TMC) at the interface, where interfacial polymerization occurs. The reaction between PIP and TMC forms a crosslinked polyamide network with HCl as a byproduct, resulting in the formation of a polyamide selective layer at the top of the PES support. Moreover, a schematic illustration of the CTFD process is compared with conventional dip-coating. In CTFD, centrifugal acceleration drives radial spreading and rapid excess-liquid removal, promoting uniform lateral coverage and more controlled interfacial polymerization.

rejection was calculated as[8]:

$$R = 1 - {}^{c_p}/_{c_f} \tag{2}$$

where C_f and C_p are the solute concentrations (mg/L) in the feed and permeate, respectively. Tests were performed in closed-loop (no recovery, 24 h) and open-loop (high recovery, 60 h) modes.

Fouling experiments were conducted using 200 mg/L sodium alginate in a solution containing 950 mg/L NaCl, 50 mg/L $CaCl_2$, at pH 7.0, following protocols from our previous studies[62,63]. To further evaluate fouling resistance under a more complex organic-fouling condition, mixed-organic-foulant tests were also performed using sodium alginate, bovine serum albumin, and humic acid in the presence of NaCl and $CaCl_2$, as described in Fig. S9, SI[64]. The operating pressure for each modified membrane was adjusted to match the initial flux of the control membrane. Pressure normalization ensures differences in fouling behavior arise from surface properties rather than hydraulic loading. Tests were run for 96 hours at one LPM in a cross-flow system. Afterward, membranes were washed with DI water under one bar pressure for 1 hour. Permeate flux during fouling (J_{w1}) and pure water fluxes before fouling (J_{w0}) and after cleaning (J_{w2}) were recorded. To assess the antifouling performance, the following parameters were calculated: flux recovery ratio (FRR), reversible fouling resistance (R_r), irreversible fouling resistance (R_{ir}), and total flux decline ratio (R_t). Fouling parameters were calculated using the following equations[63]:

$$FRR\,(\%) = \left(\frac{J_{W2}}{J_{W0}}\right) \times 100 \tag{3}$$

$$R_r\,(\%) = \left(\frac{J_{W2} - J_{W1}}{J_{W0}}\right) \times 100 \tag{4}$$

$$R_{ir}\,(\%) = \left(\frac{J_{W0} - J_{W2}}{J_{W0}}\right) \times 100 \tag{5}$$

$$R_t\,(\%) = R_r + R_{ir} = \left(\frac{J_{W0} - J_{W1}}{J_{W0}}\right) \times 100 \tag{6}$$

Molecular dynamics simulations of thin film deposition

Atomistic MD simulations were performed using LAMMPS to compare the relative spatial distribution of PIP near the PES substrate under gravity-driven and centrifugal deposition conditions during the pre-reaction stage of the IP[65]. Because the model was intended to isolate deposition-driven monomer transport, explicit solvent molecules and the PIP–TMC

polymerization reaction were not included. Therefore, the results are interpreted as qualitative mechanistic support rather than a quantitative representation of the full IP process or final polyamide structure. Molecular structures of PIP and PES were initially constructed in ArgusLab and subsequently packed into a simulation box using Packmol, ensuring realistic atomic ratios and spatial distributions. The assembled system was then processed in the Visual Molecular Dynamics (VMD 1.9) using its TKConsole extension to generate LAMMPS-compatible input files. Topology generation and force field assignments were performed using the TopoTools plugin.

The final system consisted of a rigid, atomistically modeled PES substrate and an overlying layer of PIP monomers. The simulation box dimensions were 201 Å × 201 Å × 101 Å, comprising 17,600 atoms. Periodic boundary conditions were applied in the x and y directions, with fixed boundaries in the z direction. Implicit repulsive walls were added at the top and bottom to confine atoms and prevent escape along the z-axis. All atomic interactions were described using the OPLS-AA force field. Lennard-Jones (LJ) and Coulombic interactions, specified via lj/cut/coul/cut pair style, with cutoffs of 12 Å and 8 Å, respectively[66]. Bonded interactions, including bonds, angles, and dihedrals, were defined according to the molecular connectivity of the PIP monomer and PES.

Two deposition scenarios were modeled to compare the monomer's fate at the interface under different deposition conditions. In the conventional mode, only gravitational acceleration was considered. PIP monomers underwent Brownian motion and diffused toward the substrate solely under the influence of gravity, simulating a dip-coating deposition. In the centrifugal deposition mode, a radially outward force proportional to atomic position was applied to a predefined group of PIP atoms to emulate centrifugal acceleration during membrane fabrication. This setup simulated the enhanced radial transport of monomers away from the rotational center. Each system was equilibrated using the NVT ensemble at 300 K using the Nosé–Hoover thermostat, at a timestep of 1 fs over a total simulation time of 5 ns[67]. Trajectories were recorded every 100 steps to capture the evolution of monomer spatial distribution. Visualization and post-processing were conducted using OVITO, including top-view, cross-sectional, and 3D renderings of monomer arrangements. Comparative analysis of the two scenarios focused on evaluating monomer coverage, spatial uniformity, and deposition dynamics across the substrate. Additional simulation parameters and force group definitions are detailed in Tables S3, SI.

Data Availability

The datasets generated and/or analyzed during the current study are not publicly available due to file-size limitations and because they are maintained as internal research records, but are available from the corresponding author on reasonable request.

Received: 20 February 2026; Accepted: 14 May 2026;
Published online: 22 May 2026

References

1. He, J. et al. Molecular mechanisms of thickness-dependent water desalination in polyamide reverse-osmosis membranes. *J. Membr. Sci.* **674**, 121498 (2023).
2. Radfar, S., Taheri, P. & Moftakhari, H. Global evidence for co-variability of tidal constituents. *Environ. Res. Lett.* **21**, 024019 (2026).
3. Zhang, R. et al. Antifouling membranes for sustainable water purification: strategies and mechanisms. *Chem. Soc. Rev.* **45**, 5888–5924 (2016).
4. Jiang, S., Li, Y. & Ladewig, B. P. A review of reverse osmosis membrane fouling and control strategies. *Sci. total Environ.* **595**, 567–583 (2017).
5. Ilyas, A. & Vankelecom, I. F. Designing sustainable membrane-based water treatment via fouling control through membrane interface engineering and process developments. *Adv. Colloid Interface Sci.* **312**, 102834 (2023).
6. Werber, J. R., Osuji, C. O. & Elimelech, M. Materials for next-generation desalination and water purification membranes. *Nat. Rev. Mater.* **1**, 1–15 (2016).
7. Elimelech, M. & Phillip, W. A. The future of seawater desalination: energy, technology, and the environment. *science* **333**, 712–717 (2011).
8. Di Vincenzo, M. et al. Biomimetic artificial water channel membranes for enhanced desalination. *Nat. Nanotechnol.* **16**, 190–196 (2021).
9. McGovern, R. K. On the asymptotic flux of ultrapermeable seawater reverse osmosis membranes due to concentration polarisation. *J. Membr. Sci.* **520**, 560–565 (2016).
10. Yip, N. Y., Tiraferri, A., Phillip, W. A., Schiffman, J. D. & Elimelech, M. High performance thin-film composite forward osmosis membrane. *Environ. Sci. Technol.* **44**, 3812–3818 (2010).
11. Xu, G.-R., An, Z.-H., Zhao, H.-L. & Liu, Q. Polyamide layer modulation for PA-TFC membranes optimization: developments, mechanisms, and implications. *Sep. Purif. Technol.* **311**, 123200 (2023).
12. Liang, Y. et al. Polyamide nanofiltration membrane with highly uniform sub-nanometre pores for sub-1 Å precision separation. *Nat. Commun.* **11**, 2015 (2020).
13. Lu, X. & Elimelech, M. Fabrication of desalination membranes by interfacial polymerization: history, current efforts, and future directions. *Chem. Soc. Rev.* **50**, 6290–6307 (2021).
14. Mohammad, A. W. et al. Nanofiltration membranes review: Recent advances and future prospects. *Desalination* **356**, 226–254 (2015).
15. Sarkar, P., Wu, C., Yang, Z. & Tang, C. Y. Empowering ultrathin polyamide membranes at the water–energy nexus: strategies, limitations, and future perspectives. *Chem. Soc. Rev.* **53**, 4374–4399 (2024).
16. Li, J.-B. et al. Ultrahigh-permeance polyamide thin-film composite membranes enabled by interfacial polymerization on a macro-porous substrate toward organic solvent nanofiltration. *J. Membr. Sci.* **693**, 122342 (2024).
17. Yang, Z. et al. Mechanistic insights into the role of polydopamine interlayer toward improved separation performance of polyamide nanofiltration membranes. *Environ. Sci. Technol.* **54**, 11611–11621 (2020).
18. Bai, C. et al. Stepwise increasing TMC concentration in NF membranes fabrication for controlled PA layer thickness, compactness, and charge distribution: Maintaining high permeance, enhancing desalination, and mechanistic insights. *Sep. Purif. Technol.* **359**, 130404 (2025).
19. Ding, H. -z et al. 2D nanosheets optimized electrospray-assisted interfacial polymerization polyamide membrane with excellent separation performance. *J. Membr. Sci.* **647**, 120308 (2022).
20. Mulhearn, W. D., Oleshko, V. P. & Stafford, C. M. Thickness-dependent permeance of molecular layer-by-layer polyamide membranes. *J. Membr. Sci.* **618**, 118637 (2021).
21. Saleh, E. A. M. et al. Recent advances in thin film composite (TFC) membranes development: Materials and modification methods. *Environ. Sci.: Water Res. Technol.* **11**, 1059–1085 (2025).
22. Liu, Y. -l et al. Effect of varying piperazine concentration and post-modification on prepared nanofiltration membranes in selectively rejecting organic micropollutants and salts. *J. Membr. Sci.* **582**, 274–283 (2019).
23. Wei, X., Fan, K., Cheng, P., Liu, Y. & Xia, S. Modification of nanofiltration membranes using beta-cyclodextrin derivatives with different functional groups for enhanced removal of organic micropollutants. *Desalination* **573**, 117219 (2024).
24. Zhou, Y. et al. Support-free interfacial polymerized polyamide membrane on a macroporous substrate to reduce internal concentration polarization and increase water flux in forward osmosis. *J. Membr. Sci.* **689**, 122165 (2024).
25. Shen, K., Cheng, C., Zhang, T. & Wang, X. High performance polyamide composite nanofiltration membranes via reverse interfacial

polymerization with the synergistic interaction of gelatin interlayer and trimesoyl chloride. *J. Membr. Sci.* **588**, 117192 (2019).
26. Ding, J., Wu, H. & Wu, P. Multirole regulations of interfacial polymerization using poly (acrylic acid) for nanofiltration membrane development. *ACS Appl. Mater. Interfaces* **13**, 53120–53130 (2021).
27. Zhu, C.-Y. et al. Vacuum-assisted diamine monomer distribution for synthesizing polyamide composite membranes by interfacial polymerization. *J. Membr. Sci.* **616**, 118557 (2020).
28. Lai, G. et al. A novel interfacial polymerization approach towards synthesis of graphene oxide-incorporated thin film nanocomposite membrane with improved surface properties. *Arab. J. Chem.* **12**, 75–87 (2019).
29. Zhu, C.-Y. et al. Leveraging Janus Substrates as a Confined "Interfacial Reactor" to Synthesize Ultrapermeable Polyamide Nanofilms. *Research* **7**, 0359 (2024).
30. Zhou, Z. et al. Ultrathin polyamide membranes enabled by spin-coating assisted interfacial polymerization for high-flux nanofiltration. *Sep. Purif. Technol.* **288**, 120648 (2022).
31. Xie, T. et al. High-performance polyethyleneimine based reverse osmosis membrane fabricated via spin-coating technology. *J. Membr. Sci.* **668**, 121248 (2023).
32. Son, T. Y., Kim, T.-H. & Nam, S. Y. Crosslinked pore-filling anion exchange membrane using the cylindrical centrifugal force for anion exchange membrane fuel cell system. *Polymers* **12**, 2758 (2020).
33. Liu, F., Wang, L., Li, D., Liu, Q. & Deng, B. A review: the effect of the microporous support during interfacial polymerization on the morphology and performances of a thin film composite membrane for liquid purification. *RSC Adv.* **9**, 35417–35428 (2019).
34. Lukong, V. T., Ukoba, K. & Jen, T.-C. Review of self-cleaning TiO2 thin films deposited with spin coating. *Int. J. Adv. Manuf. Technol.* **122**, 3525–3546 (2022).
35. Freger, V. Kinetics of film formation by interfacial polycondensation. *Langmuir* **21**, 1884–1894 (2005).
36. Pilevar, M. et al. Customizing surface grafting and interlayer functionalization for PFOA separation in polyamide membranes. *Water Res. X.* **27**, 100358 (2025).
37. Taghipour, A. et al. Unveiling the impact of monomer reactivity on the morphology and functionality of thin-film composite membranes. *Chem. Eng. J.* **480**, 148028 (2024).
38. Shen, L. et al. Polyamide-based membranes with structural homogeneity for ultrafast molecular sieving. *Nat. Commun.* **13**, 500 (2022).
39. Culp, T. E. et al. Electron tomography reveals details of the internal microstructure of desalination membranes. *Proc. Natl. Acad. Sci.* **115**, 8694–8699 (2018).
40. Pacheco, F. A., Pinnau, I., Reinhard, M. & Leckie, J. O. Characterization of isolated polyamide thin films of RO and NF membranes using novel TEM techniques. *J. Membr. Sci.* **358**, 51–59 (2010).
41. Woo, S. H., Park, J. & Min, B. R. Relationship between permeate flux and surface roughness of membranes with similar water contact angle values. *Sep. Purif. Technol.* **146**, 187–191 (2015).
42. Wang, M. et al. Controlled growth of polyamide films atop homogenous and heterogeneous hydrogels using gel–liquid interfacial polymerization. *Macromol. Chem. Phys.* **220**, 1900100 (2019).
43. Tan, Z., Chen, S., Peng, X., Zhang, L. & Gao, C. Polyamide membranes with nanoscale Turing structures for water purification. *Science* **360**, 518–521 (2018).
44. Park, H. B., Kamcev, J., Robeson, L. M., Elimelech, M. & Freeman, B. D. Maximizing the right stuff: The trade-off between membrane permeability and selectivity. *Science* **356**, eaab0530 (2017).
45. Do, V. T., Tang, C. Y., Reinhard, M. & Leckie, J. O. Degradation of polyamide nanofiltration and reverse osmosis membranes by hypochlorite. *Environ. Sci. Technol.* **46**, 852–859 (2012).
46. Liu, M. et al. Carbodiimide-assisted zwitterionic modification of poly (piperazine amide) thin-film composite membrane for enhanced separation and anti-depositing performances to cationic/anionic dye aqueous solutions. *J. Hazard. Mater.* **396**, 122582 (2020).
47. Wu, M. et al. Ultrathin nanofiltration membrane with polydopamine-covalent organic framework interlayer for enhanced permeability and structural stability. *J. Membr. Sci.* **576**, 131–141 (2019).
48. Zhu, J. et al. Rapid water transport through controllable, ultrathin polyamide nanofilms for high-performance nanofiltration. *J. Mater. Chem. A* **6**, 15701–15709 (2018).
49. Mansouri, J. et al. Kinetics of support-free interfacial polymerization polyamide films by in-situ absorbance spectroscopy. *Desalination* **549**, 116349 (2023).
50. Zhu, Q.-Y. et al. Novel insight on the effect of the monomer concentration on the polypiperazine-amide nanofiltration membrane. *Ind. Eng. Chem. Res.* **61**, 5843–5852 (2022).
51. Liu, D. & Xu, T. SO3H covered nanofiltration composite membrane by taurine for selective removal of anionic solutes. *Water Supply* **25**, 684–695 (2025).
52. Zhu, C.-Y. et al. Polyamide nanofilms with linearly-tunable thickness for high performance nanofiltration. *J. Membr. Sci.* **627**, 119142 (2021).
53. Huang, J., Luo, J., Chen, X., Feng, S. & Wan, Y. New insights into effect of alkaline cleaning on fouling behavior of polyamide nanofiltration membrane for wastewater treatment. *Sci. Total Environ.* **780**, 146632 (2021).
54. Mahsa Hayatbakhsh, M. S., David Pernitsky, Subir Bhattacharjee, and Javad Hajinasiri. Treatment of an in situ oil sands produced water by polymeric membranes. *Desalination Water Treatment* **57**, (2016). https://doi.org/10.1080/19443994.2015.1069216
55. Eric M. Vrijenhoek, S. H., Menachem Elimelech. Influence of membrane surface properties on initial rate of colloidal fouling of reverse osmosis and nanofiltration membranes. *J. Membr. Sci.* **188**, 115–128 (2001).
56. Tang, C.Y., Kwon, Y.N. & Leckie, J.O. Leckie. Characterization of Humic Acid Fouled Reverse Osmosis and Nanofiltration Membranes by Transmission Electron Microscopy and Streaming Potential Measurements. *Environ. Sci. Technol.* **41**, https://doi.org/10.1021/es061322r (2006).
57. Tang, Y.-N. W. a. C. Y. Nanofiltration Membrane Fouling by Oppositely Charged Macromolecules: Investigation on Flux Behavior, Foulant Mass Deposition, and Solute Rejection. *Environ. Sci. Technol.* **45**, https://doi.org/10.1021/es202709r (2011).
58. Zhao, G. et al. Doctor-blading-assisted interfacial polymerization for green and scalable polyamide membrane fabrication. *Nat. Commun.* **16**, 10481 (2025).
59. Xue, Y.-R. et al. Polyamide nanofilms synthesized by a sequential process of blade coating-spraying-interfacial polymerization toward reverse osmosis. *Sep. Purif. Technol.* **310**, 123122 (2023).
60. Liu, Z. et al. Highly anions-selective polyamide nanofiltration membrane fabricated by rod-coating assisted interfacial polymerization. *J. Membr. Sci.* **668**, 121273 (2023).
61. Baig, U. & Waheed, A. Exploiting interfacial polymerization to fabricate hyper-cross-linked nanofiltration membrane with a constituent linear aliphatic amine for freshwater production. *NPJ Clean. Water* **5**, 46 (2022).
62. Pilevar, M. et al. Analysis of Metal–Organic Framework and Polyamide Interfaces in Membranes for Water Treatment and Antibacterial Applications. *Small Methods* **9**, 2401566 (2025).
63. Jafarian, H. et al. Synthesis of heterogeneous metal organic Framework-Graphene oxide nanocomposite membranes for water treatment. *Chem. Eng. J.* **455**, 140851 (2023).
64. Ang, W. S., Tiraferri, A., Chen, K. L. & Elimelech, M. Fouling and cleaning of RO membranes fouled by mixtures of organic foulants simulating wastewater effluent. *J. Membr. Sci.* **376**, 196–206 (2011).
65. Thompson, A. P. et al. LAMMPS-a flexible simulation tool for particle-based materials modeling at the atomic, meso, and continuum scales. *Computer Phys. Commun.* **271**, 108171 (2022).

66. Jorgensen, W. L., Maxwell, D. S. & Tirado-Rives, J. Development and testing of the OPLS all-atom force field on conformational energetics and properties of organic liquids. *J. Am. Chem. Soc.* **118**, 11225–11236 (1996).
67. Hoover, W. G. Canonical dynamics: Equilibrium phase-space distributions. *Phys. Rev. A* **31**, 1695 (1985).

Acknowledgements

This research was supported by USDA TAT-RWTS 00-69526. This paper has not been formally reviewed by USDA, and the views expressed in this document are solely those of the authors and do not necessarily reflect those of USDA. USDA does not endorse any products or commercial services mentioned in this publication. USDA had no role in the study design, data collection, analysis, decision to publish, or manuscript preparation.

Author contributions

M.D.F., H.J., and N.B. conducted the membrane fabrication and performance experiments. S.A.A., S.E.M. and Z.Z. performed characterization tests and data interpretation. Y.M. contributed to the conceptual design. A.A.S. and A.R. provided theoretical insights and guidance on polyamide formation chemistry. S.N. and A.T. contributed to analysis of membrane transport mechanisms and manuscript editing. M.S. supervised the membrane fabrication and performance testing. M.E. supervised the environmental engineering aspects and guided the overall experimental design. M.D.F. conceptualized the study, coordinated the collaboration across institutions, processed and analyzed data, and wrote the main manuscript text with input from all co-authors. All authors reviewed and approved the final manuscript.

Competing interests

The authors declare no competing interests.

Additional information

Supplementary information The online version contains supplementary material available at https://doi.org/10.1038/s41545-026-00589-0.

Correspondence and requests for materials should be addressed to Mohtada Sadrzadeh, Mark Elliott or Mostafa Dadashi Firouzjaei.

Reprints and permissions information is available at http://www.nature.com/reprints

Publisher's note Springer Nature remains neutral with regard to jurisdictional claims in published maps and institutional affiliations.

Open Access This article is licensed under a Creative Commons Attribution-NonCommercial-NoDerivatives 4.0 International License, which permits any non-commercial use, sharing, distribution and reproduction in any medium or format, as long as you give appropriate credit to the original author(s) and the source, provide a link to the Creative Commons licence, and indicate if you modified the licensed material. You do not have permission under this licence to share adapted material derived from this article or parts of it. The images or other third party material in this article are included in the article's Creative Commons licence, unless indicated otherwise in a credit line to the material. If material is not included in the article's Creative Commons licence and your intended use is not permitted by statutory regulation or exceeds the permitted use, you will need to obtain permission directly from the copyright holder. To view a copy of this licence, visit http://creativecommons.org/licenses/by-nc-nd/4.0/.

© The Author(s) 2026